

Scanning the Potential Energy Surface for Synthesis of Dendrimer-Wrapped Gold Clusters: Design Rules for True Single-Molecule Nanostructures

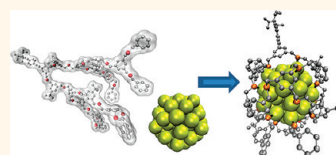
Damien Thompson,^{†,*} Jens P. Hermes,[‡] Aidan J. Quinn,[§] and Marcel Mayor^{‡,⊥}

[†]Theory Modelling and Design Centre, Tyndall National Institute, University College Cork, Cork, Ireland, [‡]Department of Chemistry, University of Basel, St. Johanns-Ring 19, CH-4056 Basel, Switzerland, [§]Micro/Nanoelectronics Centre, Tyndall National Institute, University College Cork, Cork, Ireland, and

[⊥]Institute of Nanotechnology, Karlsruhe Institute of Technology (KIT), P.O. Box 3640, D-76021 Karlsruhe, Germany

Nanostructured organic–inorganic hybrid materials may be formed *via* self-assembly of organic and inorganic components.^{1,2} Surfactant-coated gold nanoparticles (colloidal gold) in particular^{3–5} have attracted significant attention in the past decades, and their unique optical and electronic properties have led to technology applications. For example, gold nanoparticles can be used to transfer optical signals in plasmonic devices⁶ and to congregate receptor molecules in the liquid-phase sensing⁷ used in home pregnancy tests.⁸ Current research focuses on emerging applications in nanoelectronics^{9,10} and medicine.^{11–15} Gold nanoparticles may find use as functional components in printed electronics¹⁶ *via* the integration of synthesized gold nanostructures into lithographically produced structures.¹⁷ In medical diagnostics, the molecular recognition properties of low-diameter gold nanoparticle surfaces make gold particles useful platforms for analyte–receptor interactions,^{18,19} while gold particles may also be used for drug delivery applications with (surfactant-controllable) size, surface charge, and shape being the chief parameters for controlling the biological response to medicinal gold complexes.²⁰ Gold nanoparticles also have numerous current and future applications in, for example, trace analyte detection for security,²¹ as well as advanced elements for optoelectronics²² and information storage devices.²³ A key element in the rational design of gold nanoparticles is the role of ligand conformation and adsorption onto the inorganic surface in order to influence particle growth and assembly. More generally, a molecular-level control of the organic–inorganic interface is required

ABSTRACT The formation of true single-molecule complexes between organic ligands and nanoparticles is challenging and requires careful design of molecules with size, shape, and chemical properties tailored for the specific nanoparticle. Here we use computer simulations



to describe the atomic-scale structure, dynamics, and energetics of ligand-mediated synthesis and interlinking of 1 nm gold clusters. The models help explain recent experimental results and provide insight into how multidentate thioether dendrimers can be employed for synthesis of true single-ligand–nanoparticle complexes and also nanoparticle–molecule–nanoparticle “dumbbell” nanostructures. Electronic structure calculations reveal the individually weak thioether–gold bonds (325 ± 36 meV), which act collectively through the multivalent (multisite) anchoring to stabilize the ligand–nanoparticle complex (~ 7 eV total binding energy) and offset the conformational and solvation penalties involved in this “wrapping” process. Molecular dynamics simulations show that the dendrimer is sufficiently flexible to tolerate the strained conformations and desolvation penalties involved in fully wrapping the particle, quantifying the subtle balance between covalent anchoring and noncovalent wrapping in the assembly of ligand–nanoparticle complexes. The computed preference for binding of a single dendrimer to the cluster reveals the prohibitively high dendrimer desolvation barrier (1.5 ± 0.5 eV) to form the alternative double-dendrimer structure. Finally, the models show formation of an additional electron transfer channel between nitrogen and gold for ligands with a central pyridine unit, which gives a stiff binding orientation and explains the recently measured larger interparticle distances for particles synthesized and interlinked using linear ligands with a central pyridine rather than a benzene moiety. The findings stress the importance of organic–inorganic interactions, the control of which is central to the rational engineering and eventual large-scale production of functional building blocks for nano(bio)electronics.

KEYWORDS: nanoelectronics · organic–inorganic interfaces · multivalent interactions · molecular dynamics simulations · electronic structure calculations

for any application that couples organic material with metal or semiconductor substrates for integrated bionanoelectronics.^{24–26}

Linear thioether ligands have recently been shown to direct the synthesis and interlinking of gold nanoparticles in dichloromethane solvents.^{27–30} Gold particles have also been very recently synthesized in the presence of dendritic thioether ligands.³¹ The nanoparticles were formed in

* E-mail:
damien.thompson@tyndall.ie.

Received for review November 17, 2011
and accepted March 20, 2012.

Published online March 20, 2012
10.1021/nn204470g

© 2012 American Chemical Society

the presence of the dendrimer following a protocol developed by Brust as described in ref 31 with ^1H NMR showing that the particles are solely stabilized by the dendrimer. The phase transfer agent used during the synthesis of the particles was successfully removed by a repeated precipitation and centrifugation protocol, and even the excess of the dendritic ligand was removed by size exclusion chromatography.³¹ Understanding and ultimately harnessing the driving forces underlying this ligand-mediated gold nanoparticle synthesis require detailed nanoscale experiments and simulations, and so the focus of the present work is on complementing the experimental synthesis and microscopy characterization,^{27–31} using atomic-resolution computer simulations. We focus on the more promising dendritic thioether ligands, which potentially allow very precise control of both covalent and noncovalent ligand stabilization effects in nanoparticle synthesis. The simulations in the present work allow quantification of the forces underlying the assembly of dendrimer–nanoparticle complexes, namely, the multiple (individually weak, reversible) binding interactions that act collectively to give tightly woven self-correcting and self-healing assemblies. By clarifying the atom-scale structure, dynamics, and energetics of complexation, the model may be useful as a computer-aided design tool for the (eventual) generation of libraries of molecular “wrappers” for efficient synthesis of a wide range of building blocks tailored for specific nanoelectronic device applications.

The role of the adsorbed organic molecule in directing the formation of the observed narrow size distribution of ~ 1 nm diameter gold nanoparticles^{27–31} is explored *via* a combination of first-principles electronic structure calculations and atomic-resolution molecular dynamics simulations. We use the simulations to address three important questions concerning the synthesis (Figure 1): (1) How stable is a fully bound dendrimer configuration on the nanoparticle surface? Recent experiments show unchanging particle size distributions for the first- and second-generation dendrimers³¹ and so suggest that the dendrimers can fully “wrap” the particle. (2) We use the model to measure the binding and dynamics of dendrimers with different central units on the nanoparticle surface. Experiments show a significant difference in interparticle distances for linear ligands with benzene and pyridine central units.^{29,30} (3) We measure the relative stabilities of single-dendrimer and double-dendrimer complexes on the nanoparticle. Very recent experiments show predominantly 1:1 dendrimer to particle ratios for the second-generation dendrimer.³¹ This suggests the formation of only a very low population of interlinked superstructures containing three or more nanoparticles, once these dendrimers³¹ are monofunctionalized and the particles formed in their presence are interlinked using acetylene chemistry.^{29,30} Such discrete, regularly sized “dumbbells” may provide a means of

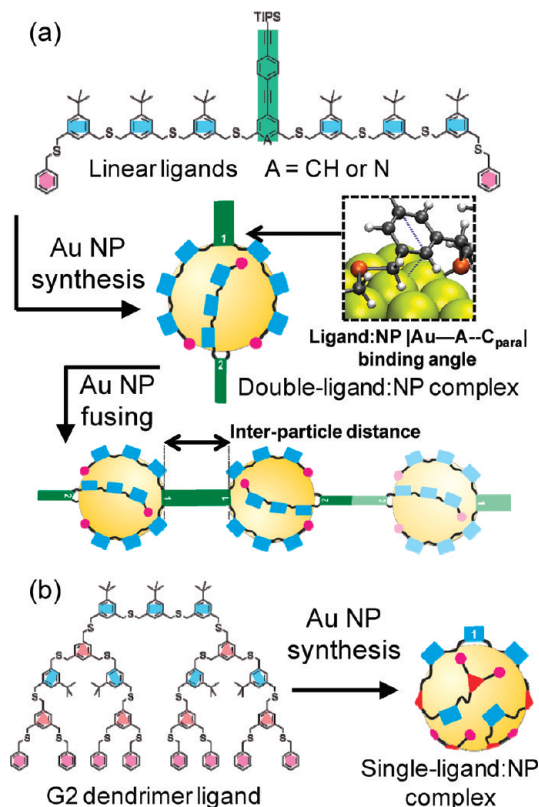


Figure 1. Sketch of the ligand-mediated nanoparticle synthesis, showing the key components and structural features. (a) Double-ligand–particle complex formed using linear ligands.^{29,30} The ligand–particle binding angle is defined by three atoms as shown: the gold atom between the two gold atoms that bind the central unit sulfurs, and two ligand ring atoms, the carbon of site “A” in benzene (nitrogen in pyridine) and the carbon *para* to A. The multiparticle chain formed *via* acetylene fusing is also shown, with the interparticle distance marked, which depends on both the length of the linker and the binding angle. (b) Single-ligand–particle complex formed using the second-generation dendrimer.³¹

cleanly bridging lithographically defined nanogaps and controlling the electron transport properties of the junction.³² The computer model confirms and extends the major features observed in the experimental synthesis and characterization of gold nanoparticles stabilized by multidentate thioether ligands, by showing how the organic template structure directs three crucial factors: the individual nanoparticle size distributions, the interparticle distances, and, we predict, the extent of particle interlinking. This new atom-scale detail may inform the synthesis of hybrid organic–inorganic materials with nanostructures and physicochemical properties tailored for specific device applications.^{33,34}

RESULTS AND DISCUSSION

We first describe the electronic structure calculations of thioether–gold bond formation and then present the larger scale molecular dynamics simulations of the room-temperature dichloromethane-solvated dendrimer–nanoparticle complexes. The simulation results are used

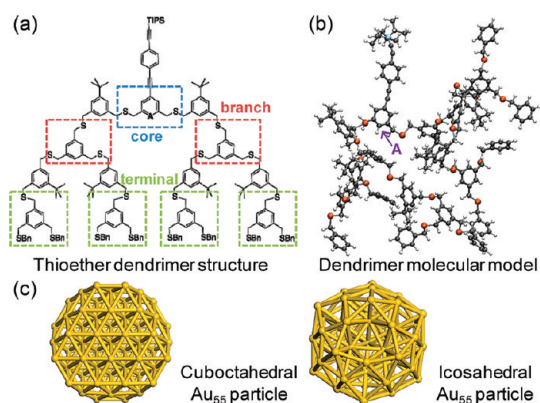


Figure 2. (a) Chemical structure of the multidentate thioether dendrimer,³¹ with positions of the two core, six branch, and 12 terminal sulfurs marked. Simulations were also performed using dendrimers with the benzene central unit replaced by a pyridine unit,³⁰ where “A” marks the site of the C–H–N substitution. (b) Dendrimer molecular model, where carbons are colored gray, hydrogen atoms are white, sulfurs are brown, and silicon of the TIPS headgroup is colored blue. This (not yet synthesized) monofunctionalized dendrimer is derived by merging the branch and terminal part of the second-generation dendrimer³¹ (panel a) with the core (central unit) of an acetylene-monofunctionalized linear ligand.^{29,30} (c) Cuboctahedral and the icosahedral Au₅₅ clusters (1.2 ± 0.1 nm diameter) used to model the synthesized gold nanoparticles (1.2 ± 0.4 nm diameter³¹).

to rationalize the experimental observations,^{28–31} and the combined simulation/experimental data are discussed in relation to the state of the art in hybrid organic–inorganic materials design and synthesis for nanoelectronics, with reference also to more general multivalent ligand–surface interactions^{35,36} relevant for nanofabrication,³⁷ molecular diagnostics,³⁸ and molecular assembly.³⁹

Computed Thioether–Gold Bond Strengths. Panels a and b of Figure 2 show the chemical structure and molecular model of the multidentate thioether dendrimer used in the present study. This model was derived from the chemical structure used in recent work³¹ including (1) the alternative pyridine central unit as yet only synthesized for the linear ligands^{29,30} and (2) the acetylene headgroup required for chemical interlinking^{29,30} of the formed dendrimer–particle complexes.³¹ Both of these variants are targets of current experiments and allow us to make predictions using the model, while providing insight into some of the recent experimental data.^{27–31} Figure 2c shows the nanoparticle shapes used to model the synthesized 1.2 ± 0.4 nm diameter gold nanoparticles,³¹ which are represented in the present study by the near-isoenergetic cuboctahedral and icosahedral 55-atom gold (Au₅₅) clusters,^{40,41} which have calculated diameters of 1.2 ± 0.1 nm. The surface of cuboctahedral Au₅₅ is composed of eight corner-sharing triangles (111) and six squares (110), while icosahedral Au₅₅ has 20 equivalent triangular fcc(111)-like faces. Figure 3 summarizes the electronic structure models used to describe bond formation between the thioether

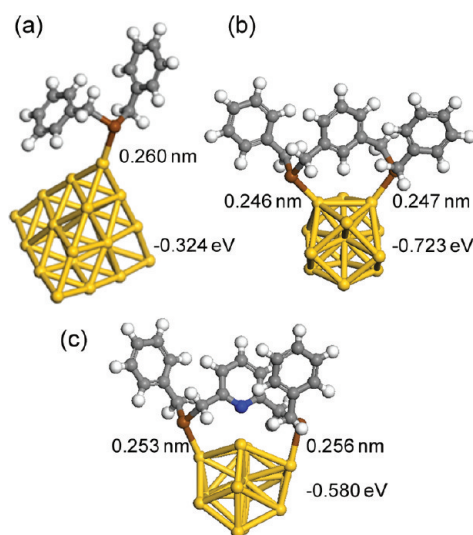


Figure 3. Complexes used to calculate the thioether–gold bond strength. (a) *T_d* tetrahedral Au₂₀ cluster, with four 10-atom triangular faces exhibiting face-centered cubic (fcc) packing. (b and c) *I_h* icosahedral Au₁₃ cluster, which contains 20 three-atom triangles. The same atom representation is used as in Figure 2b. Representative fragments of the dendrimer thioether anchor groups were used as shown: benzyl thioether (panel a) and extended benzene-core (panel b) and pyridine-core (panel c) dithioether moieties. Calculated S–Au bond lengths and molecule binding energies are given.

groups and the gold nanoparticle surface. Given the local nature of the thioether–gold bonding and the computational effort required to compute full ligand–Au₅₅ complexes,^{40–42} we use smaller Au₂₀ and Au₁₃ clusters to perform a series of adsorption calculations with different representative dendrimer building blocks and particle (111) and (110) faces to estimate the dendrimer–particle bonding energy per thioether group. As shown by the computed electronic binding energies given in Figure 3, the thioether groups make weak bonds to gold, with an average bond strength of just 325 ± 36 meV averaged over the three representative structures. The similarity in the computed bond strengths indicates only a minor dependence on the fine details of the dendrimer model (size of the representative fragment used for the electronic structure calculation, choice of benzene or pyridine central unit) and the nanoparticle surface geometry ((111) or (110) faces, geometry of the Au–S bonds). The adsorption energy is subchemisorption at approximately 0.3 eV. By comparison, methylthiomethane has a binding energy to gold of approximately 0.5 eV.⁴³

The computed thioether bond strength is substantially weaker than a 1.7 eV alkanethiol–gold bond,⁴⁴ which has two important consequences for the dendrimer-mediated gold nanoparticle synthesis. First, there is scope for self-correction in the dendrimer–gold complexation with the thioether sulfurs able to distribute themselves on the surface *via* quasi-reversible S–Au bonds so as to obtain favorable

dendrimer conformations. These dendrimer rearrangements on the surface may be accompanied by Au surface diffusion or place-exchange “hopping”,⁴⁵ which has a very low barrier (<1 eV),⁴⁶ that may be further lowered by thioether adsorption. Identification of any consequent dendrimer-directed nanoparticle distortions, defects, or gold adlayer formation⁴⁷ would require very high-resolution imaging and/or significantly larger electronic structure calculations, beyond the scope of the present study.

The second important consequence of the computed weak individual thioether–gold bond strengths is that formation of multiple bonds between the nanoparticle and the multivalent dendrimer, in this case a multidentate thioether dendrimer with 20 sulfur anchor groups, will drive the adsorption energy of the complex as a whole toward a more strongly bound, effectively chemisorbed state. Taking the estimate of 325 meV per thioether–gold bond, one fully bound dendrimer or multiple partially bound dendrimers, *e.g.*, two half-bound dendrimers, will provide an effective bond strength of 7 eV, the equivalent of four Au–alkanethiol chemical bonds. The payoff between favorable multivalent attachment and unfavorable dendrimer wrapping penalties (conformational strain plus desolvation costs) may then be used to identify thermodynamically favorable binding modes⁴⁸ for the dendrimer–nanoparticle complexes, as described below. The high effective concentration^{49,50} of unbound thioether anchor groups close to the nanoparticle surface will drive the complex toward also a *kinetically* stable multivalently bound assembly of the (individually weak) thioether–gold bonds.

Finally, it is important to note that the electronic ligand–particle binding calculations were performed for small benzene/pyridine thioether molecules adsorbed on gold clusters under vacuum at 0 K, which serves as a first approximation to the experimental dichloromethane-solvated dendrimer–nanoparticle structures synthesized in the room-temperature experiments (and modeled explicitly in the present work using classical molecular dynamics). As discussed below, a complex balance of ligand–surface chemical bonding and van der Waals’s interactions directs the assembly of the dendrimer-wrapped nanoparticle, and both types of interaction depend on the topography of the nanoparticle surface. Therefore, we extract the estimated bond strength of 325 ± 36 meV over three representative structures; experimentally, we may expect also some complexation geometries with thioether–gold bond strengths outside this range due to, for example, gold surface defects/adatoms and solvent-mediated dendrimer–gold interactions. More details on Au–S bonding calculations, including long-range effects, thermal effects, and a survey of bond strengths as a function of Au coordination in the cluster and sulfur coordination in the molecule, are given in Supporting Information section S1.

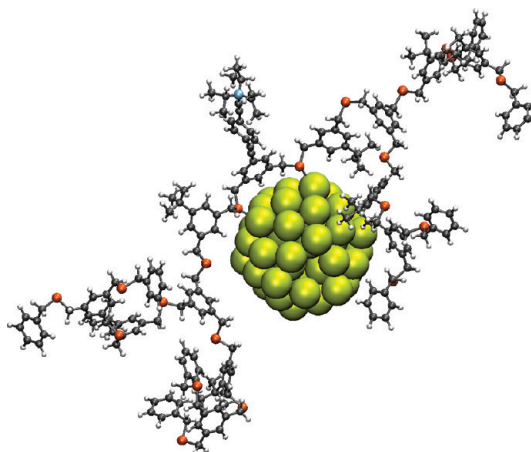


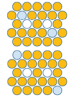
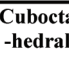
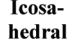
Figure 4. Representative dendrimer–gold complex model. In this case the dendrimer is bound using two core thioether–gold bonds with the gold nanoparticle atoms shown as van der Waals’s spheres. The complex is immersed in a large box of dichloromethane molecules (11 nm wide), to model the solvated dendrimer–gold complex.

Computed Dendrimer–Nanoparticle Net Complexation Energies. Figure 4 shows one representative complex used to describe the structure, dynamics, and energetics of the dendrimer–nanoparticle assembly in dichloromethane. Thirty-six dendrimer-coated gold nanoparticle models (listed in Table 1) were used to determine the stabilities of 1:1 and 2:1 dendrimer–nanoparticle complexes. Their relative stabilities indicate a very low probability for binding of a second dendrimer to exposed areas of some of the 1:1 dendrimer–nanoparticle complexes to form 2:1 dendrimer–nanoparticle complexes, providing an explanation for the measured low molecular weight of organic coats on the synthesized nanoparticles.³¹ Overall, the atom-scale simulations complement the experiments *via* identification of the principal dendrimer binding modes and thus the ideal dendrimer size required for the dendrimer-mediated gold nanoparticle synthesis.

The net adsorption energy of each solvated dendrimer–gold complex is expressed as the sum of the favorable binding interaction and unfavorable wrapping penalty. The favorable binding interactions for each assembly mode are quantified from the sum of the electronic thioether–gold bonding energies calculated above, which are assumed to be additive,⁴⁸ plus the dendrimer–nanoparticle van der Waals interactions. The unfavorable wrapping penalty inherent in dendrimer complexation is estimated as the sum of dendrimer conformational penalties and both dendrimer and gold desolvation penalties, in each case relative to reference solvated but noncomplexed dendrimer and nanoparticle models.

The data in Table 1 show that the net complexation energy fluctuates around zero for all binding modes, indicating a rather flat potential energy surface for dendrimer–particle complexation with many different

TABLE 1. Computed Dendrimer–Nanoparticle Net Complexation Energies (eV) for a Range of Single-Dendrimer (1:1) and Double-Dendrimer (2:1) Cluster Complexes in Dichloromethane^a

Nanoparticle shape	Binding mode	Electronic binding	van der Waals binding	Total binding	Dendrimer penalty	Desolvation penalty	Total penalty	Net complexation
Single-dendrimer:nanoparticle complexes								
	Two core	-0.7 (0.1)	-0.2 (0.1)	-0.8 (0.1)	-0.4 (0.5)	+1.0 (0.6)	+0.6 (0.6)	-0.3 (0.6)
		-0.7 (0.1)	-0.1 (0.0)	-0.8 (0.1)	+0.2 (0.6)	+0.3 (0.9)	+0.5 (0.9)	-0.3 (1.0)
	Two core + two branch (configuration A)	-1.3 (0.1)	-0.3 (0.1)	-1.6 (0.1)	-0.1 (0.6)	+1.8 (0.8)	+1.6 (0.8)	0.0 (0.8)
		-1.3 (0.1)	-0.4 (0.1)	-1.7 (0.1)	+0.5 (0.6)	+1.3 (0.9)	+1.8 (0.9)	+0.1 (0.9)
	Two core + two branch (configuration B)	-1.3 (0.1)	-0.3 (0.1)	-1.6 (0.1)	0.0 (0.6)	+1.6 (0.8)	+1.6 (0.8)	0.0 (0.9)
		-1.3 (0.1)	-0.2 (0.1)	-1.5 (0.1)	+0.4 (0.6)	+0.6 (0.9)	+1.0 (0.9)	-0.5 (0.9)
	Two core + two branch (configuration C)	-1.3 (0.1)	-0.3 (0.1)	-1.6 (0.1)	-0.1 (0.6)	+1.6 (0.8)	+1.6 (0.9)	0.0 (0.9)
		-1.3 (0.1)	-0.4 (0.1)	-1.7 (0.1)	+0.1 (0.6)	+1.0 (0.9)	+1.2 (0.9)	-0.5 (0.9)
Two core + six branch	-2.6 (0.3)	-0.6 (0.1)	-3.2 (0.3)	+0.2 (0.6)	+2.6 (0.8)	+2.7 (0.8)	-0.4 (0.8)	
	-2.6 (0.3)	-0.5 (0.1)	-3.1 (0.3)	+0.4 (0.6)	+2.0 (0.9)	+2.4 (0.9)	-0.8 (1.0)	
Two core + six branch + four terminal	-3.9 (0.4)	-0.6 (0.1)	-4.5 (0.4)	-0.4 (0.6)	+4.7 (0.9)	+4.3 (0.9)	-0.3 (1.1)	
	-3.9 (0.4)	-0.7 (0.1)	-4.6 (0.5)	-0.3 (0.6)	+4.5 (0.8)	+4.2 (0.9)	-0.4 (0.9)	
Two core + six branch + twelve terminal	-6.5 (0.7)	-0.8 (0.1)	-7.3 (0.7)	-0.5 (0.6)	+8.0 (0.6)	+7.4 (0.7)	+0.1 (1.0)	
	-6.5 (0.7)	-0.8 (0.1)	-7.3 (0.7)	-0.8 (0.6)	+7.8 (0.9)	+7.1 (0.9)	-0.2 (1.0)	
Double-dendrimer:nanoparticle complexes								
	Two core	-0.7 (0.1)	-0.1 (0.0)	-0.8 (0.1)	0.0 (0.6)	+0.8 (0.9)	+0.7 (0.9)	0.0 (1.1)
		-0.7 (0.1)	-0.1 (0.0)	-0.8 (0.1)	0.0 (0.6)	+0.8 (1.0)	+0.8 (1.1)	0.0 (1.1)
	Two core + two branch (configuration A)	-1.3 (0.1)	-0.2 (0.1)	-1.5 (0.1)	-0.1 (0.6)	+1.7 (1.0)	+1.6 (1.0)	+0.1 (1.0)
		-1.3 (0.1)	-0.2 (0.0)	-1.5 (0.1)	0.0 (0.6)	+1.3 (0.9)	+1.3 (0.9)	-0.2 (1.1)
	Two core + two branch (configuration D)	-1.3 (0.1)	-0.4 (0.1)	-1.7 (0.1)	0.0 (0.6)	+2.0 (0.8)	+1.9 (0.8)	+0.3 (1.0)
		-1.3 (0.1)	-0.4 (0.1)	-1.7 (0.1)	+0.1 (0.6)	+1.7 (0.9)	+1.8 (0.9)	+0.1 (1.0)
Two core + six branch	-2.6 (0.3)	-0.4 (0.1)	-3.0 (0.3)	0.0 (0.6)	+2.9 (0.8)	+2.9 (0.8)	-0.1 (1.1)	
	-2.6 (0.3)	-0.4 (0.1)	-3.0 (0.4)	-0.2 (0.6)	+3.1 (0.9)	+2.9 (0.9)	-0.2 (1.1)	
Two core + six branch + four terminal	-3.9 (0.4)	-0.6 (0.1)	-4.5 (0.4)	-0.4 (0.6)	+4.8 (0.8)	+4.4 (0.8)	-0.1 (1.0)	
	-3.9 (0.4)	-0.6 (0.1)	-4.5 (0.4)	-0.4 (0.9)	+4.4 (0.8)	+4.1 (0.9)	-0.4 (1.2)	
	Two core	-1.3 (0.1)	-0.4 (0.1)	-1.7 (0.1)	-1.2 (0.8)	+3.8 (1.1)	+2.6 (1.1)	+0.9 (1.3)
		-1.3 (0.1)	-0.2 (0.0)	-1.5 (0.1)	-0.3 (1.0)	+2.5 (1.5)	+2.2 (1.5)	+0.6 (1.7)
	Two core + two branch (configuration D)	-2.6 (0.3)	-0.7 (0.1)	-3.3 (0.3)	-1.7 (1.0)	+6.4 (1.5)	+4.6 (1.5)	+1.3 (1.8)
		-2.6 (0.3)	-0.7 (0.1)	-3.3 (0.3)	-1.5 (1.0)	+6.0 (1.5)	+4.5 (1.5)	+1.2 (1.8)
Two core + six branch	-5.2 (0.6)	-0.9 (0.1)	-6.1 (0.6)	-3.1 (1.0)	+11.0 (1.4)	+7.8 (1.4)	+1.8 (1.7)	
	-5.2 (0.6)	-0.9 (0.1)	-6.1 (0.7)	-3.2 (1.0)	+10.6 (1.4)	+7.5 (1.4)	+1.4 (1.8)	
	Two core	-1.3 (0.1)	-0.3 (0.1)	-1.6 (0.1)	-2.2 (1.0)	+5.5 (1.4)	+3.2 (1.4)	+1.6 (1.8)
		-1.3 (0.1)	-0.4 (0.1)	-1.7 (0.2)	-1.5 (1.0)	+4.4 (1.4)	+2.9 (1.4)	+1.2 (1.8)
	Two core + two branch (configuration D)	-2.6 (0.3)	-0.4 (0.1)	-3.0 (0.4)	-1.9 (1.0)	+6.1 (1.7)	+4.2 (1.7)	+1.2 (1.9)
		-2.6 (0.3)	-0.6 (0.1)	-3.3 (0.3)	-1.7 (1.0)	+6.4 (1.5)	+4.8 (1.6)	+1.6 (1.9)
Two core + six branch	-5.2 (0.6)	-0.8 (0.1)	-6.0 (0.6)	-2.3 (1.0)	+9.4 (1.2)	+7.1 (1.3)	+1.1 (1.9)	
	-5.2 (0.6)	-0.8 (0.1)	-6.0 (0.6)	-2.5 (1.0)	+10.1 (1.3)	+7.6 (1.3)	+1.6 (1.8)	

^aFor each binding mode, the computed energies for the dendrimer with benzene central unit is given in the top row, with the corresponding pyridine-core dendrimer values given underneath. Structure-averaged uncertainty (standard deviation) for each energy is given in parentheses. Electronic binding energies were calculated as described in Figure 3 and supporting text, with further details in Supporting Information section S1.3. The other terms were computed from the final 5 ns (2000 structures) of 10 ns room-temperature molecular dynamics for each complex. A minus sign indicates net stabilization of the complex relative to reference noncomplexed states. Rounding all energy values to one decimal place gives in some cases apparent discrepancies of 0.1 eV between totals and their components. Sketched in the insets are binding configurations **A–D** on the gold cluster surface, with core binding sites colored white and branch binding sites colored blue. The binding modes refer to the extent of thioether–gold bonding and are described using the dendrimer unit nomenclature given in Figure 2a.

competing binding modes. Each binding configuration will have a population distribution scaled according to its range of net complexation energies. Examination of the mean net complexation energies for single- and double-dendrimer complexes, E_1 and E_2 , respectively, averaged over all structures and plotted in Figure 5, is instructive. The plot indicates a sharp destabilization for double- vs single-dendrimer complexation to the nanoparticle, with an estimated mean barrier to double-dendrimer binding, $E_2 - E_1 \approx 1.5 \pm 0.5$ eV,

obtained by averaging over all the single- and double-dendrimer data points in Figure 5. Examination of the energy components in Table 1 shows that this barrier arises principally from increased wrapping penalties in the double-dendrimer complexes, which are roughly double the value for single-dendrimer complexes. Conversely, the dendrimer–gold van der Waals binding energies show little dependence on the number of bound dendrimers, comparing single- and double-dendrimer complexes with similar overall numbers of

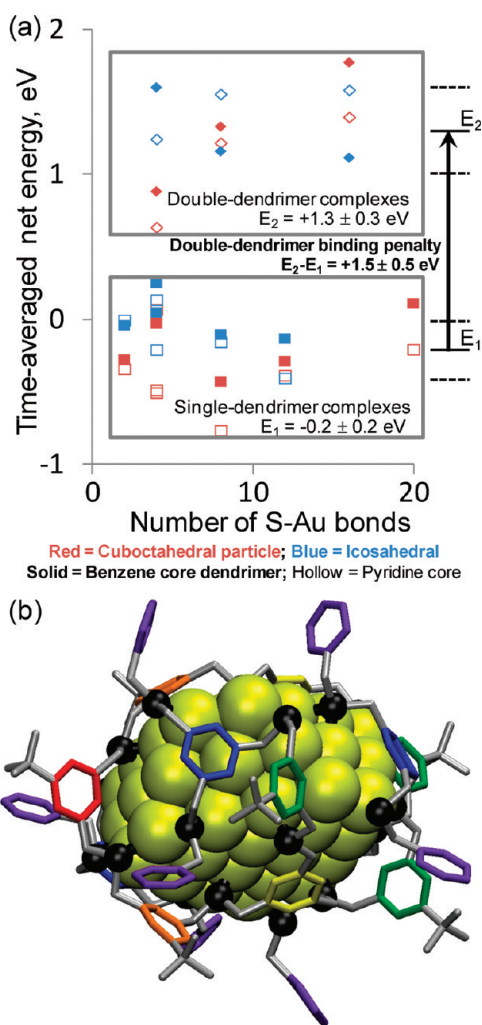


Figure 5. (a) Computed time-averaged net complexation energies for single- and double-dendrimer–nanoparticle complexes with increasing numbers of gold–thioether bonds. Data in red are for the cuboctahedral particle, and data in blue are for the icosahedral particle. Solid and hollow data points are used for the dendrimers with benzene and pyridine central units, respectively. The gray boxes show the clustering of data points for single- and double-dendrimer complexes, with the arrow showing the 1.5 ± 0.5 eV barrier for binding of a second dendrimer. (b) One representative computed single-dendrimer–gold complex. In this picture the dendrimer carbon backbone is shown as gray sticks and thioether sulfurs are black spheres. Hydrogen atoms and the dichloromethane solvent molecules are omitted for clarity. Phenyls are colored according to the visible spectrum, starting from the central unit (red) and radiating outward through to the terminal groups (violet).

S–Au bonds. Similarly, the spread in the data points in terms of particle shape, central unit, and binding configurations (where configurations **A**, **B**, **C**, and **D** denote the alternative surface grafting schemes sketched in the inset figures in Table 1) is generally <1 eV for each binding extent.

The major driver toward single-dendrimer complexes then is the enlarged desolvation contribution that mitigates against binding of the second dendrimer. As shown in Table 1, the net desolvation cost is

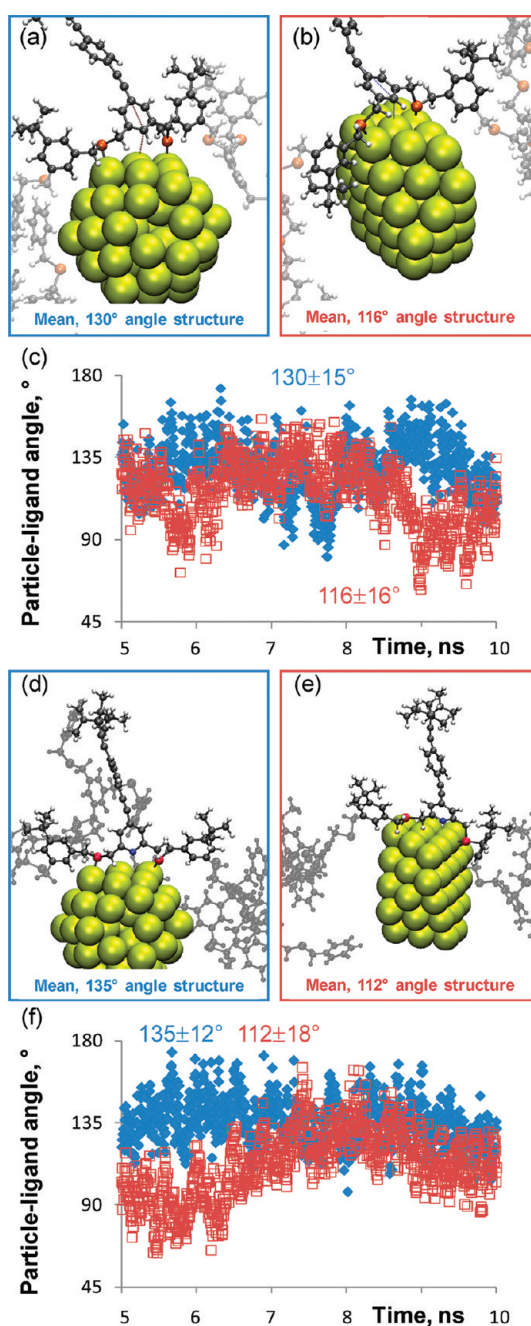


Figure 6. Computed ligand–nanoparticle complexation geometries. (a and b) Representative structures formed using the dendrimer with the benzene central unit, with timelines (c) showing the angle formed between the nanoparticle surface and the dendrimer central unit (as sketched in Figure 1). Data in blue are for the icosahedral particle, and data in red are for the cuboctahedral particle, with timelines showing values sampled over the final 5 ns of 10 ns molecular dynamics trajectories. (d and e) Structures formed with the pyridine central unit and (f) angle timelines. Only the two core sulfurs are bound to the nanoparticle surface in order to allow direct comparison of linear and dendritic ligands; the complexation geometries do not change significantly upon connection of more or all sulfurs.

partially offset by dendrimer “penalties” that become negative for the double-dendrimer–particle complexes and, hence, provide an additional stabilizing

dendrimer energy due to favorable van der Waals interactions between the two dendrimers. The net total penalty however remains large and positive, shifting the double-dendrimer complexes to net positive time-averaged complexation energies, meaning that they will constitute a minor state in the synthesis, in agreement with the experimental microscopy and thermogravimetric data.³¹ The synthesis thus “self-terminates” in the majority of cases at the 1:1 dendrimer–gold complexes. Future experiments will fuse the complexes *via* diacetylene bond formation to form 2:2 dimer complexes, or “dumbbells”.^{29,30} The computed barrier to binding two dendrimers on one gold cluster (2:1) and hence the small number of states with interlinked $2n:n$ superstructures predict a very low population of multi-particle networks of trimeric and higher order structures.

In summary, the energetic data in Table 1 show that the dendrimer desolvation energy dictates the number of ligands comprising the moderately polar nanoenvironment of thioether groups in which the gold nanoparticle is stabilized in bulk dichloromethane. Hence it may prove possible to tune the extent of ligand coverage by using solvents of different dielectric constant and/or different ligand anchor groups. It may prove possible to direct the nanoparticle size by tuning also with respect to the desolvation energy of the nanoparticle itself. The information provided by chemical bonding/fusing in this directed assembly is reminiscent of the chemical scission step used between successive rounds of spontaneous assembly/wrapping that provides control of collagen synthesis in complex, multiphase biological environments.⁵¹ Routes to manipulate and ultimately control directed assembly in dendrimer-mediated nanoparticle synthesis could allow for simultaneous production of a wide variety of nanoparticle complexes of different type, size, and shape stabilized by different types and numbers of ligands. In the nearer term the attainment of such control could aid development of ultrasensitive and specific sensing of target molecules for medical diagnostics and therapeutics. Further details on calculated dendrimer–gold wrapping dynamics are given in the Supporting Information. Section S2 describes the more open dendrimer conformations but more solvent-shielded gold complex structures formed in methanol, a more polar solvent than the dichloromethane used in the experiments. Section S3 shows that wrapping *via* binding through core and then peripheral sulfurs is energetically favored over an alternative “feet first” orientation. Section S4 shows that wrapping of a larger 1.4 nm cluster, Au₆₉, shows a similar balance between wrapping and desolvation forces, with a slightly better, ~ 1 eV stabilization of the complex due to reduced desolvation penalties for the more splayed dendrimer conformation on the larger particle.

Structural Features of Dendrimer-Coated Gold Nanoparticles.

In contrast to the dendrimers, the linear ligands were already monofunctionalized and used to couple

nanoparticles to superstructures.^{29,30} The models of functional dendrimers are now used to explain the differences in interparticle spacing found for linear ligands, as we assume the geometry of the central unit, either a pyridine or benzene moiety, does not depend on the ligand structure. For this simulation only the central two thioethers were bound to the nanoparticle. Even if more thioethers are bound to the surface, the computed angle does not change. This nicely enables the comparison of linear and dendritic ligands. Ligand–particle complexation geometries were computed and are shown in Figure 6 with representative structures and timelines showing the angle formed between the plane of the central unit benzene (or pyridine) and the gold surface. The ligand–particle binding angle (sketched in Figure 1) is the angle formed between the plane of the ligand central ring and the gold surface. The computed angles are used to calculate the interparticle distances by simply multiplying the length of the calculated OPE-type linker, 2.8 nm, and the cosine of the measured time-averaged tilt of the core-to-particle angle away from an ideal, perpendicularly oriented central unit (which would be 180°, as sketched in Figure 1). Interparticle distances of 1.8 ± 0.5 and 2.0 ± 0.4 nm were obtained for icosahedral particles with benzene and pyridine central units, respectively. For the cuboctohedral particle the distances are 1.2 ± 0.7 and 1.0 ± 0.8 nm. The complete range of experimentally measured interparticle distances for linear acetylene-functionalized octadentate thioether ligands is 0.7–3.1 nm,³⁰ peaking at 1.5 ± 0.5 nm for the benzene central unit (ligand B2 in ref 30) and 2.5 ± 0.3 nm for the pyridine moiety (P2 in ref 30). The computed angles are thus consistent with the observed interparticle distances³⁰ and span the full range of observed distances (for a freely rotating core group; the quantum mechanical origin of the pyridine constraint that gives the observed peak shift to 2.5 nm³⁰ is discussed below), indicating that a mixture of nanoparticle shapes is fabricated. Cuboctohedral gold particles are ~ 1 eV less stable than icosahedral particles,⁴¹ and so taken together, the calculations and experiments suggest that the gold clusters produced in dendrimer-mediated synthesis may show deviations from perfect crystallinity. Furthermore, gold atom migration to “fill” the dendrimer wrapper *via* gold adlayer formation may be enabled by the weak individual thioether–gold chemical bonds (Figure 3) and, from the energetic data in Table 1, may be expected to give mutually compensating van der Waals and desolvation interactions. This would provide a significant population of nanoparticles that are slightly larger than the 1.2 ± 0.1 nm Au₅₅ clusters, in agreement with the broader shoulders at higher diameters in the measured nanoparticle size distributions.^{29–31}

The computed ligand–particle angles show a negligible dependence on central unit type, benzene or pyridine (Figure 6), indicating that the experimentally

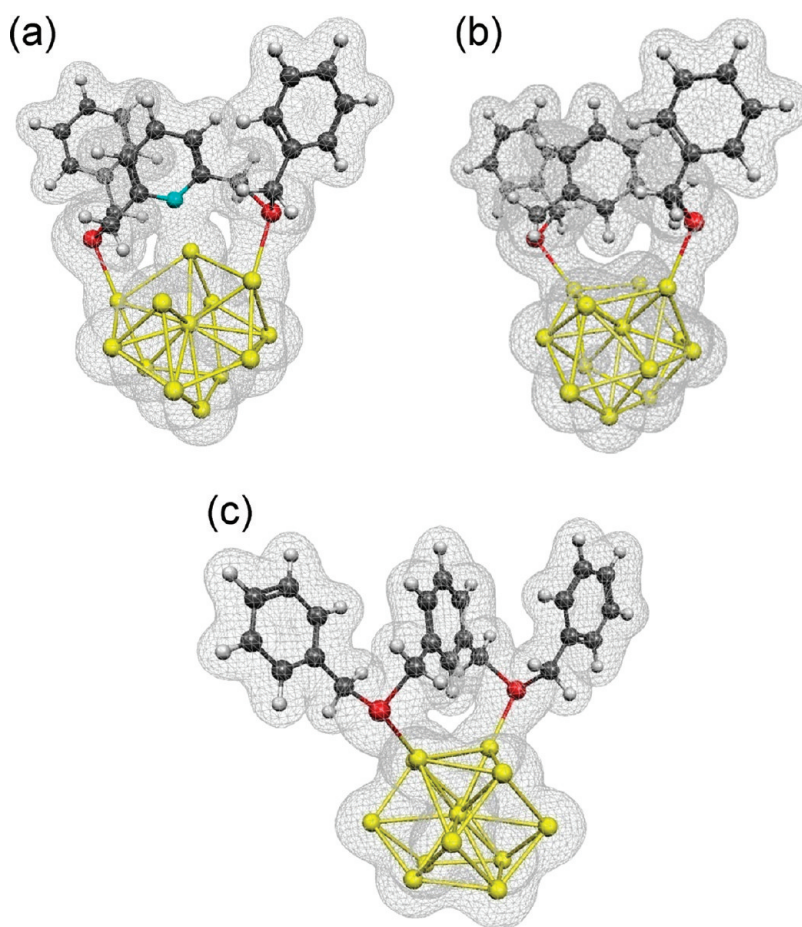


Figure 7. (a) The three charge transfer channels for pyridine thioether surface adsorption. (b and c) The two charge transfer channels for benzene thioether adsorption, which features no binding through the benzene central unit. Panel (b) shows the structure formed by replacing the pyridine moiety in the gold-bound pyridine thioether structure with benzene and reoptimizing the complex, while panel (c) shows an alternative benzene dithioether binding mode. Electron density maps (isodensity 0.001 e/au^3) were calculated from the electronic structures described in the text.

observed core-dependent interparticle separations³⁰ do not originate primarily from differences in noncovalent interactions with the particle surface, as modeled in the molecular dynamics simulations. Rather, as shown in Figure 7, the origin of the different interparticle separations is largely electronic. Figure 7 shows the three charge transfer channels for pyridine thioether surface adsorption, with charge donation of 2×0.11 electron charges from the sulfur sites ($S_{2p} \rightarrow Au_{7d}$) and a small back-donation from the surface of 0.04 electron charges to the nitrogen site ($Au_{7d} \rightarrow N_{2p}$). These degrees and sites of charge transfer were estimated from natural population analysis⁵² of the computed electronic structures in Figure 7, which are the two dithioether structures from Figure 3 and also an additional control simulation that replaced the central pyridine moiety of pyridine dithioether with benzene and reoptimized the complex. Conversely, only two charge transfer channels exist for benzene thioether adsorption, which features charge donation of $2 \times 0.16 \text{ e}^-$ from the two sulfur sites but *no* bonding through the benzene central unit.

This striking difference in reactivity and hence binding geometry for ligands with benzene and pyridine central units is further explained by analysis of the local softness,⁵³ which measures the nucleophilicity and electrophilicity of atoms in the adsorbate molecules. The computed local softness indices $s(r)$ indicate as expected highly reactive thioether sites with sulfur electron-donor powers $s^-(r)$ of 0.09 and 0.10 au each in benzene and pyridine dithioether, respectively. All other sites exhibit negligible $s^-(r)$ values, $\leq 0.01 \text{ au}$. On the other hand computed local electrophilicity indices show very delocalized electron-acceptor sites in benzene dithioether with sulfurs exhibiting $s^+(r) = 0.02 \text{ au}$ and all other atoms $\leq 0.01 \text{ au}$, while pyridine dithioether on the other hand shows $s^+(r) = 0.04 \text{ au}$ on nitrogen, 0.02 au on the *ortho* and *para* ring carbons, and 0.02 au on sulfurs, with all other atoms $\leq 0.01 \text{ au}$. Hence the flexible central unit for benzene-based ligands compared with the stiff, more immobilized central unit for pyridine-based ligands manifests itself in the larger interparticle distances measured for linear ligands with pyridine central units.³⁰ As this difference

was explained just by using the two core sulfurs of the ligand, we are optimistic that we can transfer the experimental finding to future interlinking reactions of functional nanoparticles stabilized by dendrimers.

CONCLUSIONS

The present study provides the atom-scale mechanism underlying ligand-mediated gold nanoparticle synthesis. The computational analysis based on dendrimer–nanoparticle binding vs wrapping penalties explains some key results from the experimental synthesis and characterization. Namely, the observed particle size distribution ranges,^{29–31} the 1:1 dendrimer to particle ratio found for the second-generation dendrimer,³¹ the lack of dependence of nanoparticle size on dendrimer generation,³¹ and the control of interparticle distance distributions found for nanoparticles stabilized and interlinked by linear thioether ligands.³⁰ We also use the calculated structures to predict the formation of discrete gold nanoparticle dumbbells upon future diacetylene coupling of monofunctional nanoparticles. More generally, the calculated properties may be useful for rational design of novel dendrimer structures with chemical structures and stereochemistry optimized for the

production of nanoparticle size and shape distributions as required for specific nanoelectronic device components. In the longer term, we hope that the data will contribute toward the atom-scale engineering of organic molecule-based “wrappers” for the development of building blocks with highly controllable electronic properties.

Further simulation and experimental studies will provide more details on the role of nanoparticle surface effects in ligand-directed nanoparticle synthesis, including gold atom defects, gold diffusion, and formation of gold adlayers. Rational control of the organic–inorganic interaction is key, and so deeper understanding of the atom-scale features of the interfaces in hybrid superstructures will aid efforts to design libraries of organic wrappers. Further scientific and technological advances in the application of low-dimensional nanostructures as device components depend on the ability to organize them in complex one- or multidimensional functional architectures, and so atomic-scale descriptions will continue to guide syntheses and speed up development of new materials for next-generation applications in electronics, health, and energy.

MATERIALS AND METHODS

This section contains further technical details on the simulation protocols used; the main features of the models were summarized at the beginning of the Results section.

Electronic Structure Calculations. The cuboctahedral Au₅₅ nanoparticle was generated from the bulk Au crystal structure, and its electronic structure calculated using the Gaussian03 code⁵⁴ with the B3LYP⁵⁵ hybrid Hartree–Fock–density functional theory (DFT) wave function and the relativistic LANL2DZ basis set. The geometry of the icosahedral particle, generated using the same protocol as described above, was kindly provided by Françoise Remacle from an earlier study.⁴¹ To quantify the strength of ligand anchoring on the gold nanoparticle surface, smaller representative models were used to describe the local thioether–gold interaction, as shown in Figure 3. The tetrahedral Au₂₀ cluster has four 10-atom fcc (111) faces, and the icosahedral Au₁₃ cluster has a rougher local arrangement of gold atoms, containing 20 three-atom triangles with a dihedral angle of 138.19° between planes, while benzyl thioether together with extended benzene-core and pyridine-core dibenzyl thioether moieties represents the local dendrimer molecular structure around the thioether sulfur binding sites. The adsorbate molecules and molecule–surface complexes were described with the B3LYP wave function and a large valence double- ζ polarized basis set named 6-31G(d,p) for all atoms other than gold, which required the relativistic LANL2DZ basis set. The three models shown in Figure 3 gave stable binding configurations *via* nuclear relaxation to root-mean-square (rms) atomic forces and displacements below 0.0003 and 0.0012 au, respectively. The electronic binding energy was calculated in the usual way, by subtracting the electronic energies of the optimized isolated molecule and cluster from that of the molecule–cluster complex. Further details on the Au–S bond strength estimate are given in Supporting Information section S1.3. Local softness indices $s(r)$ ⁵³ were calculated from the product of the molecular softness S (the inverse of half the HOMO–LUMO gap; S values of 0.37 and 0.39 au respectively

were computed for benzene and pyridine thioether) and atom-sited Fukui functions obtained by subtracting natural population analysis (NPA)⁵² charges in neutral and cationic/anionic benzene and pyridine dithioether molecules to identify strong electron donor/acceptor sites. The electron density surfaces shown in Figure 7 were produced using MOLEKEL Unix version 4.3.⁵⁶

Molecular Dynamics Simulations. The electronic structure of the dichloromethane (DCM) solvent and thioether-based dendrimers was described using existing force field data.^{57,58,48} A total of 12 912 DCM molecules formed a stable cubic box of edge length 11.16 ± 0.01 nm, following 10 ns of constant pressure temperature dynamics with periodic boundary conditions. The corresponding volume per molecule of 0.11 nm^3 gives a density of $1.30 \text{ g} \cdot \text{cm}^{-3}$, in good agreement with the experimental value of $1.33 \text{ g} \cdot \text{cm}^{-3}$, and gives computed DCM radial distribution functions (not shown) in excellent agreement with literature diffraction data.⁵⁹ Solvated dendrimer–nanoparticle complexes were generated by immersing each complex in a DCM box and deleting overlapping DCM molecules. Each model was relaxed using 2000 steps of steepest descent minimization with respect to the CHARMM22 force field⁵⁸ and then brought to room temperature by gradually raising the temperature from 0 to 295 K over 2 ns of dynamics while simultaneously loosening positional constraints on the dendrimer heavy atoms. Gold nanoparticle atoms were constrained to their starting positions throughout the simulations, corresponding to the quantum mechanical optimized nanoparticle geometry described above, with classical gold–sulfur bond potentials for the nanoparticle–thioether linkages fitted to the average bond length obtained in the gold–thioether electronic structure calculations, 0.251 ± 0.005 nm. Each of the 36 models listed in Table 1 was then subjected to 10 ns dynamics runs to allow formation of well-equilibrated solvated, room-temperature dendrimer–gold complexes. This corresponds to over $0.4 \mu\text{s}$ of dynamics in all, 432 ns, composed of 72 ns for equilibration plus 360 ns of equilibrated dynamics. Additional control simulations featuring solvated but noncomplexed dendrimer and nanoparticle

models provided reference values for the computation of the wrapping penalties in Table 1. Further details on the model geometry and force field parameters are given in Supporting Information section S1.

Molecular Langevin dynamics were performed using the NAMD program⁶⁰ with Ewald summation used to calculate the electrostatic interactions and a 2 fs time step used for dynamics by constraining covalent bonds to hydrogen *via* the ShakeH algorithm.⁶¹ Image generation and Tcl script-based trajectory analysis was performed using the VMD program.⁶²

Conflict of Interest: The authors declare no competing financial interest.

Acknowledgment. We acknowledge support for this research from the European Community's Seventh Framework Programme (FP7/2007-2013) under grant agreement number 213382 (FUNMOL). We acknowledge Science Foundation Ireland (SFI) for computing resources at Tyndall National Institute and SFI/Higher Education Authority for computing time at the Irish Centre for High-End Computing (ICHEC).

Supporting Information Available: Detailed methods and control simulations describing long-range interactions, thermal effects and gold/sulfur reactivity in Au–S bond formation, dendrimer wrapping around gold in a more polar methanol solvent, wrapping in a less favorable “feet first” orientation, and wrapping of a larger, 1.4 nm Au₆₉ particle. This material is available free of charge *via* the Internet at <http://pubs.acs.org>.

REFERENCES AND NOTES

- Sanchez, C.; Julian, B.; Belleville, P.; Popall, M. Applications of Hybrid Organic-Inorganic Nanocomposites. *J. Mater. Chem.* **2005**, *15*, 3559–3592.
- van Schooneveld, M. M.; Gloter, A.; Stephan, O.; Zagonel, L. F.; Koole, R.; Meijerink, A.; Mulder, W. J. M.; de Groot, F. M. F. Imaging and Quantifying the Morphology of an Organic-Inorganic Nanoparticle at the Sub-nanometre Level. *Nat. Nanotechnol.* **2010**, *5*, 538–544.
- Rao, C. N. R.; Kulkarni, G. U.; Thomas, P. J.; Edwards, P. P. Metal Nanoparticles and their Assemblies. *Chem. Soc. Rev.* **2000**, *29*, 27–35.
- Daniel, M. C.; Astruc, D. Gold Nanoparticles: Assembly, Supramolecular Chemistry, Quantum-Size-Related Properties, and Applications toward Biology, Catalysis, and Nanotechnology. *Chem. Rev.* **2004**, *104*, 293–346.
- Parker, J. F.; Fields-Zinna, C. A.; Murray, R. W. The Story of a Monodisperse Gold Nanoparticle: Au₂₅L₁₈. *Acc. Chem. Res.* **2010**, *43*, 1289–1296.
- Maier, S. A.; Atwater, H. A. Plasmons: Localization and Guiding of Electromagnetic Energy in Metal/Dielectric Structures. *J. Appl. Phys.* **2005**, *98*, 011101.
- Astruc, D.; Daniel, M. C.; Ruiz, J. Dendrimers and Gold Nanoparticles as Exo-receptors Sensing Biologically Important Anions. *Chem. Commun.* **2004**, 2637–2649.
- Bangs, L. B. New Developments in Particle-Based Immunoassays: Introduction. *Pure Appl. Chem.* **1996**, *68*, 1873–1879.
- Zheng, Y. H.; Lalander, C. H.; Bach, U. Nanoscale Force Induced Size-Selective Separation and Self-Assembly of Metal Nanoparticles: Sharp Colloidal Stability Thresholds and hcp Ordering. *Chem. Commun.* **2010**, *46*, 7963–7965.
- Homberger, M.; Simon, U. On the Application Potential of Gold Nanoparticles in Nanoelectronics and Biomedicine. *Philos. T. R. Soc. A* **2010**, *368*, 1405–1453.
- Chanda, N.; Kattumuri, V.; Shukla, R.; Zambre, A.; Katti, K.; Upendran, A.; Kulkarni, R. R.; Kan, P.; Fent, G. M.; Casteel, S. W.; *et al.* Bombesin Functionalized Gold Nanoparticles Show *in vitro* and *in vivo* Cancer Receptor Specificity. *Proc. Natl. Acad. Sci. U. S. A.* **2010**, *107*, 8760–8765.
- You, C. C.; Chompoosor, A.; Rotello, V. M. The Biomacromolecule-Nanoparticle Interface. *Nano Today* **2007**, *2*, 34–43.
- Shan, J.; Tenhu, H. Recent Advances in Polymer Protected Gold Nanoparticles: Synthesis, Properties and Applications. *Chem. Commun.* **2007**, 4580–4598.
- Eck, W.; Craig, G.; Sigdel, A.; Ritter, G.; Old, L. J.; Tang, L.; Brennan, M. F.; Allen, P. J.; Mason, M. D. PEGylated Gold Nanoparticles Conjugated to Monoclonal F19 Antibodies as Targeted Labeling Agents for Human Pancreatic Carcinoma Tissue. *ACS Nano* **2008**, *2*, 2263–2272.
- Eck, W.; Nicholson, A. I.; Zentgraf, H.; Semmler, W.; Bartling, S. Anti-CD4-targeted Gold Nanoparticles Induce Specific Contrast Enhancement of Peripheral Lymph Nodes in X-ray Computed Tomography of Live Mice. *Nano Lett.* **2010**, *10*, 2318–2322.
- Perelaer, J.; Smith, P. J.; Mager, D.; Soltman, D.; Volkman, S. K.; Subramanian, V.; Korvink, J. G.; Schubert, U. S. Printed Electronics: The Challenges Involved in Printing Devices, Interconnects, and Contacts Based on Inorganic Materials. *J. Mater. Chem.* **2010**, *20*, 8446–8453.
- Jiang, L.; Wang, W. C.; Fuchs, H.; Chi, L. F. One-Dimensional Arrangement of Gold Nanoparticles with Tunable Interparticle Distance. *Small* **2009**, *5*, 2819–2822.
- So, C. R.; Kulp, J. L.; Oren, E. E.; Zareie, H.; Tamerler, C.; Evans, J. S.; Sarikaya, M. Molecular Recognition and Supramolecular Self-Assembly of a Genetically Engineered Gold Binding Peptide on Au{111}. *ACS Nano* **2009**, *3*, 1525–1531.
- Kang, B.; Mackey, M. A.; El-Sayed, M. A. Nuclear Targeting of Gold Nanoparticles in Cancer Cells Induces DNA Damage, Causing Cytokinesis Arrest and Apoptosis. *J. Am. Chem. Soc.* **2010**, *132*, 1517–1519.
- Aillon, K. L.; Xie, Y. M.; El-Gendy, N.; Berkland, C. J.; Forrest, M. L. Effects of Nanomaterial Physicochemical Properties on *in vivo* Toxicity. *Adv. Drug Delivery Rev.* **2009**, *61*, 457–466.
- Peng, G.; Tisch, U.; Adams, O.; Hakim, M.; Shehada, N.; Broza, Y. Y.; Billan, S.; Abdah-Bortnyak, R.; Kuten, A.; Haick, H. Diagnosing Lung Cancer in Exhaled Breath using Gold Nanoparticles. *Nat. Nanotechnol.* **2009**, *4*, 669–673.
- Maye, M. M.; Gang, O.; Cotlet, M. Photoluminescence Enhancement in CdSe/ZnS-DNA Linked-Au Nanoparticle Heterodimers Probed by Single Molecule Spectroscopy. *Chem. Commun.* **2010**, *46*, 6111–6113.
- Kim, S. J.; Lee, J. S. Flexible Organic Transistor Memory Devices. *Nano Lett.* **2010**, *10*, 2884–2890.
- Ruiz-Hitzky, E.; Darder, M.; Aranda, P.; Ariga, K. Advances in Biomimetic and Nanostructured Biohybrid Materials. *Adv. Mater.* **2010**, *22*, 323–336.
- Laaksonen, P.; Kivioja, J.; Paananen, A.; Kainlauri, M.; Kontturi, K.; Ahopelto, J.; Linder, M. B. Selective Nanopatterning Using Citrate-Stabilized Au Nanoparticles and Cysteine-Modified Amphiphilic Protein. *Langmuir* **2009**, *25*, 5185–5192.
- Noy, A. Bionanoelectronics. *Adv. Mater.* **2011**, *23*, 807–820.
- Hermes, J. P.; Sander, F.; Peterle, T.; Mayor, M. From Ligand-Stabilized Gold Nanoparticles to Hybrid Organic-Inorganic Superstructures. *Chimia* **2011**, *65*, 219–222.
- Peterle, T.; Leifert, A.; Timper, J.; Sologubenko, A.; Simon, U.; Mayor, M. Multidentate Thioether Ligands Coating Gold Nanoparticles. *Chem. Commun.* **2008**, 3438–3440.
- Peterle, T.; Ringler, P.; Mayor, M. Gold Nanoparticles Stabilized by Acetylene-Functionalized Multidentate Thioether Ligands: Building Blocks for Nanoparticle Superstructures. *Adv. Funct. Mater.* **2009**, *19*, 3497–3506.
- Hermes, J. P.; Sander, F.; Peterle, T.; Cioffi, C.; Ringler, P.; Pfohl, T.; Mayor, M. Direct Control of the Spatial Arrangement of Gold Nanoparticles in Organic-Inorganic Hybrid Superstructures. *Small* **2011**, *7*, 920–929.
- Hermes, J. P.; Sander, F.; Peterle, T.; Urbani, R.; Pfohl, T.; Thompson, D.; Mayor, M. Gold Nanoparticles Stabilized by Thioether Dendrimers. *Chem.—Eur. J.* **2011**, *17*, 13473–13481.
- Moth-Poulsen, K.; Bjornholm, T. Molecular Electronics with Single Molecules in Solid-State Devices. *Nat. Nanotechnol.* **2009**, *4*, 551–556.
- Rybtchinski, B. Adaptive Supramolecular Nanomaterials Based on Strong Noncovalent Interactions. *ACS Nano* **2011**, *5*, 6791–6818.
- Qian, M. C.; Reber, A. C.; Ugrinov, A.; Chaki, N. K.; Mandal, S.; Saavedra, H. M.; Khanna, S. N.; Sen, A.; Weiss, P. S. Cluster-Assembled Materials: Toward Nanomaterials with Precise Control over Properties. *ACS Nano* **2010**, *4*, 235–240.

35. Mammen, M.; Choi, S. K.; Whitesides, G. M. Polyvalent Interactions in Biological Systems: Implications for Design and Use of Multivalent Ligands and Inhibitors. *Angew. Chem., Int. Ed.* **1998**, *37*, 2755–2794.
36. Perl, A.; Gomez-Casado, A.; Thompson, D.; Dam, H. H.; Jonkheijm, P.; Reinhoudt, D. N.; Huskens, J. Gradient-Driven Motion of Multivalent Ligand Molecules along a Surface Functionalized with Multiple Receptors. *Nat. Chem.* **2011**, *3*, 317–322.
37. Mulder, A.; Huskens, J.; Reinhoudt, D. N. Multivalency in Supramolecular Chemistry and Nanofabrication. *Org. Biomol. Chem.* **2004**, *2*, 3409–3424.
38. Kim, C.; Agasti, S. S.; Zhu, Z. J.; Isaacs, L.; Rotello, V. M. Recognition-Mediated Activation of Therapeutic Gold Nanoparticles inside Living Cells. *Nat. Chem.* **2010**, *2*, 962–966.
39. Kostiainen, M. A.; Kasyutich, O.; Cornelissen, J. J. L. M.; Nolte, R. J. M. Self-Assembly and Optically Triggered Disassembly of Hierarchical Dendron-Virus Complexes. *Nat. Chem.* **2010**, *2*, 394–399.
40. Schmid, G. The Relevance of Shape and Size of Au-55 Clusters. *Chem. Soc. Rev.* **2008**, *37*, 1909–1930.
41. Periyasamy, G.; Remacle, F. Ligand and Solvation Effects on the Electronic Properties of Au-55 Clusters: A Density Functional Theory Study. *Nano Lett.* **2009**, *9*, 3007–3011.
42. Pei, Y.; Shao, N.; Gao, Y.; Zeng, X. C. Investigating Active Site of Gold Nanoparticle Au₅₅(PPh₃)₁₂Cl₆ in Selective Oxidation. *ACS Nano* **2010**, *4*, 2009–2020.
43. Lim, J. K.; Kim, I. H.; Kim, K. H.; Shin, K. S.; Kang, W.; Choo, J.; Joo, S. W. Adsorption of Dimethyl Sulfide and Methanethiolate on Ag and Au Surfaces: Surface-Enhanced Raman Scattering and Density Functional Theory Calculation Study. *Chem. Phys.* **2006**, *330*, 245–252.
44. Ulman, A. Formation and Structure of Self-Assembled Monolayers. *Chem. Rev.* **1996**, *96*, 1533–1554.
45. Wu, S. M.; Gonzalez, M. T.; Huber, R.; Grunder, S.; Mayor, M.; Schonenberger, C.; Calame, M. Molecular Junctions Based on Aromatic Coupling. *Nat. Nanotechnol.* **2008**, *3*, 569–574.
46. Strachan, D. R.; Johnston, D. E.; Guiton, B. S.; Datta, S. S.; Davies, P. K.; Bonnell, D. A.; Johnson, A. T. C. Real-Time TEM Imaging of the Formation of Crystalline Nanoscale Gaps. *Phys. Rev. Lett.* **2008**, *100*, 056805.
47. Jadzinsky, P. D.; Calero, G.; Ackerson, C. J.; Bushnell, D. A.; Kornberg, R. D. Structure of a Thiol Monolayer-Protected Gold Nanoparticle at 1.1 Angstrom Resolution. *Science* **2007**, *318*, 430–433.
48. Thompson, D. Free Energy Balance Predicates Dendrimer Binding Multivalency at Molecular Printboards. *Langmuir* **2007**, *23*, 8441–8451.
49. Huskens, J.; Mulder, A.; Auletta, T.; Nijhuis, C. A.; Ludden, M. J. W.; Reinhoudt, D. N. A Model for Describing the Thermodynamics of Multivalent Host-Guest Interactions at Interfaces. *J. Am. Chem. Soc.* **2004**, *126*, 6784–6797.
50. Thompson, D. The Effective Concentration of Unbound Ink Anchors at the Molecular Printboard. *J. Phys. Chem. B* **2008**, *112*, 4994–4999.
51. Jones, R. A. L. *Soft Machines: Nanotechnology and Life*; Oxford University Press: Oxford, 2007 (paperback); Chapter 5, pp 117–120.
52. Reed, A. E.; Weinstock, R. B.; Weinhold, F. Natural Population Analysis. *J. Chem. Phys.* **1985**, *83*, 735–746.
53. Yang, W. T.; Parr, R. G. Hardness, Softness, and the Fukui Function in the Electronic Theory of Metals and Catalysis. *Proc. Natl. Acad. Sci. U. S. A.* **1985**, *82*, 6723–6726.
54. Frisch, M. J.; Trucks, G. W.; Schlegel, H. B.; Scuseria, G. E.; Robb, M. A.; Cheeseman, J. R.; Scalmani, G.; Barone, V.; Mennucci, B.; Petersson, A.; et al. *Gaussian 09*; Gaussian, Inc.: Wallingford, CT, 2009.
55. Becke, A. D. Density-Functional Thermochemistry 0.3. The Role of Exact Exchange. *J. Chem. Phys.* **1993**, *98*, 5648–5652.
56. Varetto, U. *MOLEKEL* Version 4.3; Swiss National Supercomputing Centre: Manno (Switzerland).
57. Richardi, J.; Fries, P. H.; Krienke, H. Liquid Properties of Tetrahydrofuran and Methylene Chloride via the Molecular Hypernetted Chain Approximation. *J. Phys. Chem. B* **1998**, *102*, 5196–5201.
58. MacKerell, A. D.; Bashford, D.; Bellott, M.; Dunbrack, R. L.; Evanseck, J. D.; Field, M. J.; Fischer, S.; Gao, J.; Guo, H.; Ha, S.; et al. All-Atom Empirical Potential for Molecular Modeling and Dynamics Studies of Proteins. *J. Phys. Chem. B* **1998**, *102*, 3586–3616.
59. Balint, S.; Bako, I.; Grosz, T.; Megyes, T. Structure of Liquid Methylene Chloride: Molecular Dynamics Simulation Compared to Diffraction Experiments. *J. Mol. Liq.* **2007**, *136*, 257–266.
60. Phillips, J. C.; Braun, R.; Wang, W.; Gumbart, J.; Tajkhorshid, E.; Villa, E.; Chipot, C.; Skeel, R. D.; Kale, L.; Schulten, K. Scalable Molecular Dynamics with NAMD. *J. Comput. Chem.* **2005**, *26*, 1781–1802.
61. Ryckaert, J. P.; Ciccotti, G.; Berendsen, H. J. C. Numerical-Integration of Cartesian Equations of Motion of a System with Constraints - Molecular-Dynamics of N-Alkanes. *J. Comput. Phys.* **1977**, *23*, 327–341.
62. Humphrey, W.; Dalke, A.; Schulten, K. VMD: Visual Molecular Dynamics. *J. Mol. Graph.* **1996**, *14*, 33–38.